Quantum dynamics of ultrafast charge transfer at an oligothiophene-fullerene heterojunction

Cite as: J. Chem. Phys. **137**, 22A540 (2012); https://doi.org/10.1063/1.4751486
Submitted: 01 June 2012 • Accepted: 26 August 2012 • Published Online: 19 September 2012

Hiroyuki Tamura, Rocco Martinazzo, Matthias Ruckenbauer, et al.

Quantum dynamics of ultrafast charge transfer at an oligothiophene-fullerene heterojunction

Hiroyuki Tamura,[1] Rocco Martinazzo,[2] Matthias Ruckenbauer,[3] and Irene Burghardt[3,a)]
[1]*WPI-Advanced Institute for Material Research, Tohoku University, 2-1-1 Katahira, Aoba-ku, Sendai 980-8577, Japan*
[2]*Dipartimento di Chimica, Università degli Studi di Milano, v. Golgi 19, 20133 Milano, Italy*
[3]*Institut für Physikalische und Theoretische Chemie, Goethe Universität Frankfurt, Max-von-Laue-Str. 7, D-60438 Frankfurt am Main, Germany*

(Received 1 June 2012; accepted 26 August 2012; published online 19 September 2012)

Following up on our recent study of ultrafast charge separation at oligothiophene-fullerene interfaces [H. Tamura, I. Burghardt, and M. Tsukada, J. Phys. Chem. C **115**, 10205 (2011)], we present here a detailed quantum dynamical perspective on the charge transfer process. To this end, electron-phonon coupling is included non-perturbatively, by an explicit quantum dynamical treatment using the multi-configuration time-dependent Hartree (MCTDH) method. Based upon a distribution of electron-phonon couplings determined from electronic structure studies, a spectral density is constructed and employed to parametrize a linear vibronic coupling Hamiltonian. The diabatic coupling is found to depend noticeably on the inter-fragment distance, whose effect on the dynamics is here investigated. MCTDH calculations of the nonadiabatic transfer dynamics are carried out for the two most relevant electronic states and 60 phonon modes. The electron transfer process is found to be ultrafast and mediated by electronic coherence, resulting in characteristic oscillatory features during a period of about 100 fs. © *2012 American Institute of Physics*. [http://dx.doi.org/10.1063/1.4751486]

I. INTRODUCTION

Elementary photoinduced processes in organic functional materials and biomaterials are often found to be ultrafast, involving energy and charge transfer on a time scale of femtoseconds to picoseconds. Thus, the initial exciton dissociation processes at organic semiconductor heterojunctions typically occur within tens or hundreds of femtoseconds, while the subsequent step of photocurrent generation can be significantly slower.[1–11] The relevant time scales are strongly influenced by electron-phonon interactions mediating the transfer processes. In organic materials, these interactions are far more pronounced than in inorganic semiconductors.

In view of the above, a quantum mechanical treatment of the combined electronic and nuclear evolution is necessary, especially to understand the primary photoinduced events occurring on ultrafast time scales. This is underscored by the direct experimental observation of quantum coherence associated with these processes, both in biological systems and in functional materials.[12–14] Besides mechanistic clarifications, accurate theoretical predictions can help identify the key factors that contribute to the efficiency of the transfer processes. However, the theoretical treatment of quantum dynamical processes in high-dimensional systems exhibiting static and dynamic disorder poses a considerable challenge. Various approaches are currently pursued[15] to account with reasonable precision both for the relevant electronic structure and dynamical properties, including density functional calculations,[16] on-the-fly electronic structure approaches,[17–20] kinetic descriptions,[21] and quantum or mixed quantum-classical dynamical calculations based upon appropriate model Hamiltonians.[22–25]

Here, we address the elementary charge transfer events in an oligothiophene-fullerene complex that serves as a model system for donor-acceptor bulk heterojunctions consisting of poly-3-hexylthiophene (P3HT) and phenyl-C_{61} butyric acid methyl ester (PCBM) components.[26–31] For this material, comparatively high conversion efficiencies have been reported, and the initial charge separation has been found to occur on an ultrafast time scale – as fast as 50–200 fs.[27,28,32,33] The global efficiency of the transfer processes that eventually lead to photocurrent generation is determined by the energetics of the heterojunction material, the efficiency of exciton migration towards the interface region, the details of the interface morphology, losses due to geminate recombination (presumably the most important loss factor), and the efficiency of electron and hole transport once the charge separation has taken place.[15,31]

The approach adopted here focuses upon the ultrafast transfer events and involves a suitably parametrized vibronic coupling Hamiltonian, based upon the electronic structure calculations reported in Ref. 34. Here, an *ab initio* based diabatization[35] procedure was carried out leading to a linear vibronic coupling (LVC) form of the electron-phonon Hamiltonian.[23,36,37] The LVC model is the simplest diabatic model Hamiltonian which accounts for the relevant excited electronic states in a qualitatively correct fashion, taking into account the complex topologies of intersecting surfaces, in particular at conical intersections. Generalizations of this Hamiltonian involve the inclusion of higher-order terms in a systematic Taylor expansion, or the embedding of the locally linearized structure into a correct representation of the global

a)E-mail: burghardt@theochem.uni-frankfurt.de.

adiabatic potential surfaces. For the purpose of describing the high-dimensional polymer systems under consideration, the LVC model is appropriate since essentially small-amplitude motions are involved.

In the present analysis, the LVC model will be combined with an *ab initio* generated spectral density of phonon modes, and the multi-configuration time-dependent Hartree (MCTDH) method[38] will be used for the time propagation involving more than 50 phonon modes. The coherent nature of the transfer process, the role of the inter-fragment distance coordinate, and the relative importance of the oligothiophene vs. fullerene modes, will be addressed. The present study complements an initial dynamical analysis which was presented in Ref. 34.

The remainder of the paper is organized as follows. Section II describes the vibronic coupling model and spectral density analysis upon which the quantum dynamical calculations are based. Section III gives a brief account of the MCTDH method as applied in the present context. Section IV presents a detailed analysis and discussion, and finally, Sec. V presents conclusions.

II. VIBRONIC COUPLING MODEL

In Ref. 34, a LVC model was parametrized based upon supermolecular electronic structure calculations for an oligothiophene(OT_4)-fullerene (C_{60}) complex, see Fig. 1. In this donor-acceptor complex, a photogenerated excitonic donor state (OT_4^*-C_{60}, henceforth denoted XT) is coupled to a charge separated state (OT_4^+-C_{60}^-, henceforth denoted CT). A long-range corrected time-dependent density functional[39] method was employed to characterize the relevant states at vertically excited and state-optimized geometries, and a diabatization procedure[35] was carried out by projecting upon reference wavefunctions of pure excitonic vs. charge transfer character.

Further, electron-phonon coupling constants were determined from the displacements between the XT and CT minima along the normal mode coordinates, see Fig. 2.[34] The latter were obtained by normal mode analysis for the separate OT_4^+ and C_{60}^- fragments, with $N = 264$ modes overall. The distribution of electron-phonon couplings shown in Fig. 2 features the characteristic high-frequency C=S and C=C stretching modes of the OT_4^+ and C_{60}^- moieties around 0.2 eV (~1600 cm^{-1}). The low-frequency modes below ~0.1 eV (~800 cm^{-1}) correspond to OT_4^+ in-plane bending modes and the radial fullerene H_g modes.[40]

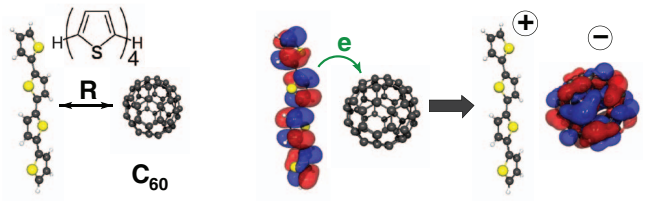

FIG. 1. Left panel: Schematic illustration of the oligothiophene(OT_4)-fullerene (C_{60}) complex considered in this work. Right panel: Illustration of the electron transfer process, with the LUMO orbitals of the OT_4 and C_{60} moieties shown.

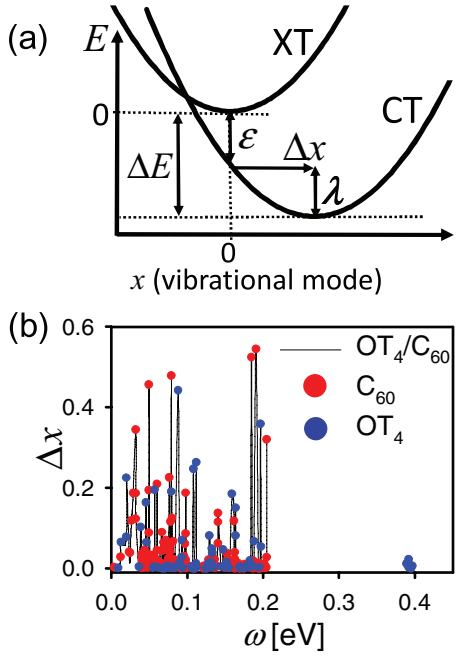

FIG. 2. (a) Schematic illustration of the XT/CT potential crossing. Here, $\epsilon = \Delta_{\text{XT-CT}}$ is the vertical XT-CT gap at the XT equilibrium geometry (see Eq. (2)), $\lambda = \sum_{i=1}^{N}(\kappa_i^2/2\omega_i)$ is the CT reorganization energy (see Eq. (4)), $\Delta E = \Delta_{\text{XT-CT}} + \lambda$ is the energetic offset between the minima of the two diabatic potentials, and Δx is the phonon-induced shift of the equilibrium geometry. (b) Phonon-induced shifts Δx for the vibrational normal modes of the OT_4^+ and C_{60}^- fragments, respectively. Reprinted with permission from H. Tamura, I. Burghardt, and M. Tsukada, J. Phys. Chem. C **115**, 10205 (2011). Copyright 2011 American Chemical Society.

As pointed out in Ref. 34, the reorganization energy λ (see Fig. 2), i.e., the difference between the CT energy at the XT minimum and the CT minimum, respectively, is small, $\lambda \sim 0.13$ eV, as has been observed experimentally.[41] Within a Marcus theory perspective, the XT $\rightarrow$ CT charge transfer process belongs to the inverted-region and near activationless regime,[42] which is typically associated with a rapid charge transfer. In line with this, the charge separation rate was found to be temperature independent.[32]

A. Linear vibronic coupling Hamiltonian

The LVC Hamiltonian that was parametrized for the XT and CT states by the above calculations, is given as follows:

$$\hat{H} = \hat{H}_0 + \hat{H}_R + \hat{H}_B, \tag{1}$$

where $\hat{H}_0$ refers to the electronic part, $\hat{H}_R$ represents a part depending on the inter-fragment (R) coordinate, and $\hat{H}_B$ includes the collection of remaining intramolecular "bath" modes. The $\hat{H}_0$ part reads as follows:

$$\hat{H}_0 = -\Delta_{\text{XT-CT}}|\text{CT}\rangle\langle\text{CT}| + \gamma\left(|\text{XT}\rangle\langle\text{CT}| + |\text{CT}\rangle\langle\text{XT}|\right), \tag{2}$$

where the electronic gap $\Delta_{\text{XT-CT}}$ and the coupling γ are of the order of 0.1 eV (see Table I), and $\hat{H}_R$ is given as

$$\hat{H}_R = \frac{\omega_R}{2}(\hat{R}^2 + \hat{P}^2) + \kappa_R\hat{R}\,|\text{CT}\rangle\langle\text{CT}| + \gamma_R\hat{R}\,(|\text{XT}\rangle\langle\text{CT}| + |\text{CT}\rangle\langle\text{XT}|) \tag{3}$$

using mass and frequency weighted coordinates. The diagonal coupling parameter κ_R reflects the displacement of the

TABLE I. Parameters, quoted in eV, for the $\hat{H}_0$ and $\hat{H}_R$ portions of the Hamiltonian, see Eqs. (2) and (3).

$\Delta_{\text{XT-CT}}$	γ	γ_R	κ_R	ω_R
0.079	0.130	−0.010	0.030	0.010

CT equilibrium geometry from the XT reference geometry. The R-dependent part of the diabatic coupling, proportional to γ_R, was obtained from the diabatization procedure mentioned above, and was found to be a linear function of R to a good approximation.[34]

Finally, the bath Hamiltonian $\hat{H}_B$ represents the intrafragment modes whose couplings are assumed to be electronically diagonal, i.e., of tuning type,

$$\hat{H}_B = \sum_{i=1}^{N} \frac{\omega_i}{2}\left(\hat{x}_i^2 + \hat{p}_i^2\right) + \sum_{i=1}^{N} \kappa_i \hat{x}_i \, |\text{CT}\rangle\langle\text{CT}| + \sum_{i=1}^{N} \frac{\kappa_i^2}{2\omega_i}. \tag{4}$$

The vibronic couplings $\{\kappa_i\}$ again reflect the displacement of the CT equilibrium geometries from the XT reference geometry, and the last term on the rhs of Eq. (4) corresponds to the CT reorganization energy $\lambda = \sum_{i=1}^{N}(\kappa_i^2/2\omega_i)$. The set of $\{\kappa_i\}$ parameters are either given in terms of the *ab initio* determined normal mode couplings illustrated in Fig. 2, or else in terms of the spectral density based couplings of Eq. (7) below.

The validity of the displaced harmonic oscillator model that is implicit in the LVC approach has been confirmed for the present system by comparing normal mode frequencies with the reorganization energies obtained by geometry optimization.[34]

B. Spectral density analysis

The discrete, normal-mode based distribution of electron-phonon couplings depicted in Fig. 2 is now used to construct continuous spectral densities $J(\omega)$ which are better suited to describe the actual polymer material that is characterized by a continuous density of modes.

Following Ref. 43, a convolution with a broadening function is carried out based upon the N_0 original data of Fig. 2 (here, $N_0 = 264$). To this end, a Lorentzian envelope function is used,

$$\begin{aligned} J(\omega) &= \frac{\pi}{2}\sum_{i=1}^{N_0} \kappa_i^2 \delta(\omega - \omega_i) \\ &\simeq \frac{\pi}{2}\sum_{i=1}^{N_0} \frac{\kappa_i^2}{\pi} \frac{\Delta}{(\omega - \omega_i)^2 + \Delta^2}, \end{aligned} \tag{5}$$

where the parameter Δ determines the Lorentzian width. In the calculations reported in Sec. IV below (see Fig. 3), a reference value Δ_0 is fixed at the root-mean-square (rms) of the frequency spacings of the original data set, and a series of values $\Delta = c\,\Delta_0$ are generated by multiplication with a factor c.

Once the continuous reference spectral density has been generated, $J(\omega)$ can be re-discretized for an arbitrary number

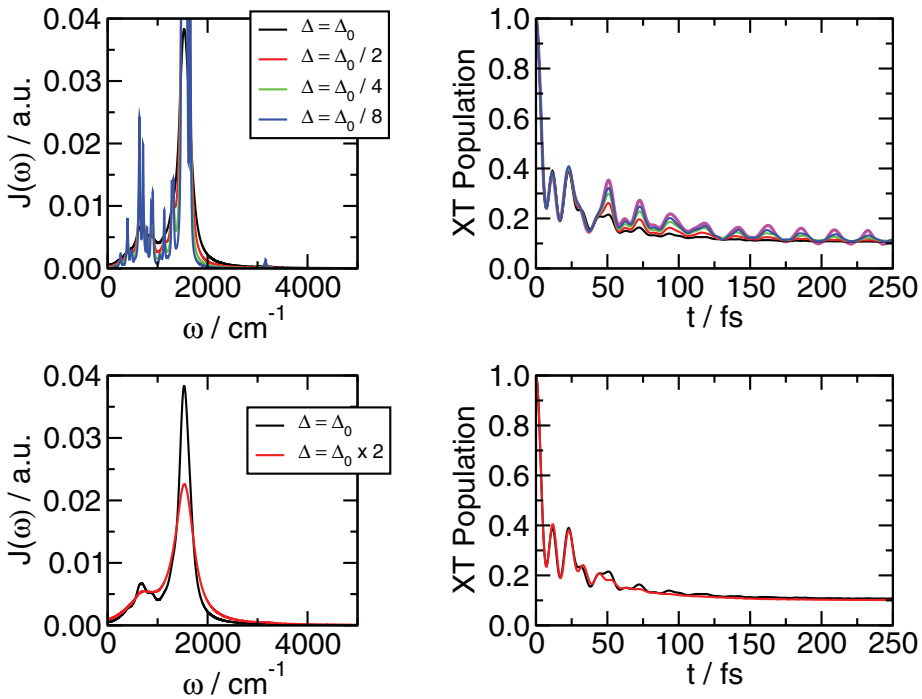

FIG. 3. Left panels: Successively broadened spectral densities, based upon a convolution of the original data shown in Fig. 2 with a Lorentzian envelope function as described in Secs. II B and IV A. Right panels: Corresponding XT state decay profiles. The magenta trace indicates the simulation result obtained with the original discretized spectral density of Fig. 2(b). While the oscillatory features beyond 50 fs tend to be washed out for the strongly broadened spectral densities, the decay on the shortest time scale (<50 fs) remains unaffected.

of N bath modes,

$$J(\omega) = \frac{\pi}{2} \sum_{i=1}^{N} \kappa_i^2 \delta(\omega - \omega_i). \tag{6}$$

The discretized coupling coefficients $\{\kappa_i\}$ of Eq. (6) are obtained as follows from the reference spectral density $J(\omega)$ of Eq. (5), given an equidistant sampling interval $\Delta\omega$:[43]

$$\kappa_i = \left(\frac{2}{\pi} J(\omega_i) \Delta\omega \right)^{1/2}. \tag{7}$$

The sampling interval defines the Poincaré recurrence period $\tau_p = 2\pi/\Delta\omega$. For times $t < \tau_p$, the observed dynamics is effectively irreversible. The calculations reported below have been carried out for $N = 60$ and $\Delta\omega = 49.4$ cm^{-1} such that the Poincaré period is given by $\tau_P = 676$ fs.

As detailed in Refs. 34 and 43, an effective mode decomposition of the spectral density can alternatively be used to obtain a re-discretization of the continuous spectral density $J(\omega)$. The results obtained from this alternative procedure are equivalent to the results reported here.

III. QUANTUM DYNAMICAL CALCULATIONS

Quantum dynamical calculations are carried out for the combined subsystem plus bath at zero temperature, using the MCTDH method.[38,44–46] In the MCTDH approach, the wavefunction is expanded in terms of Hartree products, i.e., products of time-dependent so-called single-particle functions (spf) $\varphi_j^{(\kappa)}(\mathbf{x}_\kappa, t)$,

$$\psi(\mathbf{x}_1, \ldots, \mathbf{x}_f, t) = \sum_{j_1}^{n_1} \cdots \sum_{j_f}^{n_f} A_{j_1,\ldots,j_f}(t) \prod_{\kappa=1}^{f} \varphi_{j_\kappa}^{(\kappa)}(\mathbf{x}_\kappa, t) \tag{8}$$

with the time-dependent expansion coefficients $A_{j_1,\ldots,j_f}(t)$ and time-dependent spf configurations, whose evolution is given in terms of nonlinear dynamical equations derived from the Dirac-Frenkel time-dependent variational principle. The spf's are further expanded in a so-called primitive basis, typically a discrete-variable representation.[38]

In the ansatz Eq. (8), the spf's can be either one-dimensional or multi-dimensional (so-called combined-mode spf's). In the latter case, the number of configurations is significantly reduced, which is of special importance for calculations with a large number of degrees of freedom. In the present example, where 60 modes were propagated on two non-adiabatically coupled potential surfaces, the bath modes were combined into 5-mode particles, with the number n_κ of basis functions in a given subspace ranging from 2 to 6. The R coordinate was represented by a single-mode spf with $n_\kappa = 6$. The overall number of configurations was $N_{\text{config}} = 12\,096\,000$ in the calculations reported below.

In Ref. 34, similar calculations were carried out based upon the original set of normal modes, and disregarding the dynamical effect of the inter-fragment mode R. In the present context, some focus is placed on the spectral density sampling described above, which allows for a more realistic modeling of the phonon-mediated transfer process.

IV. RESULTS AND DISCUSSION

In the following, the XT → CT transfer dynamics induced by the vibronic interactions will be analyzed in some detail. We report on MCTDH calculations for several realizations of the spectral densities Eqs. (5) and (6) that are obtained by re-discretizing the original data set as described in Sec. II B. Of particular interest is the coherent nature of the observed transfer dynamics, which could depend upon the degree of smoothing imposed by the Lorentzian filter of Eq. (5).

The MCTDH method is ideally suited to carry out this analysis since no approximations are made in the description of the nonadiabatic transfer dynamics. Thus, accurate information can be obtained about the electronically and/or vibrationally coherent nature of the transfer. The main approximation that is involved in the present calculations therefore relates to the representation of the potentials in terms of the LVC form in Eqs. (1)–(4).

Initial conditions for all calculations reported below correspond to a multidimensional wavefunction that is centered at the minimum of the XT state potential. This is justified by the observation that the reorganization energy between the ground state and the XT state is small.[34] Small displacements in the initial condition do not change the dynamics noticeably.

A. Coherent transfer dynamics

Figure 3 shows the decay of the photogenerated XT state (rhs panels), induced by a phonon distribution sampled from a series of smoothed spectral densities (lhs panels). The rise of the CT state is symmetric, i.e., $P_{\text{XT}} + P_{\text{CT}} = 1$ within the present two-state model. The XT decay is very rapid, with an initial decay component on a 10 fs time scale, and exhibits pronounced oscillatory features within the first 100–200 fs. From about 50 fs onwards, these oscillations are gradually washed out as a function of the broadening of the spectral density that is used for sampling the phonon distribution. We further note that the XT state is not entirely depleted but a residual population $P_{\text{XT}} \sim 0.1$ apparently persists beyond 250 fs.

The spectral densities that are shown in the left part of Fig. 3 are derived from the original distribution of couplings (see Fig. 2) according to the Lorentzian smoothing of

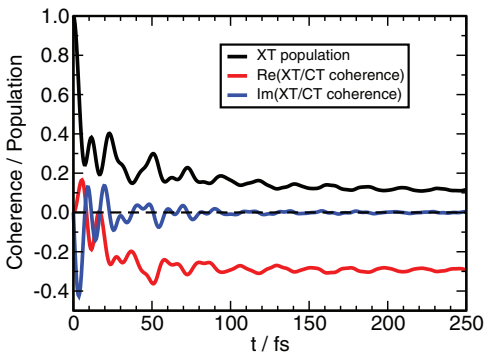

FIG. 4. Time-evolving electronic coherence, see Eq. (9), accompanying the population transfer. Real and imaginary parts are shown separately, see the discussion in Sec. IV A. The simulations were carried out for $\Delta = 0.25\Delta_0$.

Eq. (5), with $\Delta = c\Delta_0$, $c = 0.0125, 0.25, 0.5, 1, 2$. Here $\Delta_0 = 4.36\ 10^{-4}$ a.u. (96 cm^{-1}) corresponds to the rms of the sampling distance of the original data. The broadened versions of the spectral density can be taken to be a realistic representation of the spectral distribution of modes in the actual polymer material which exhibits static and dynamic disorder.

Even though the oscillatory features beyond 50 fs appear to be washed out when the strongly broadened distributions ($c = 1, 2$) are considered, the shortest time scale decay up to ~40 fs remains entirely unchanged. We are therefore led to the conclusion that the very rapid coherent dynamics on this time scale is an intrinsic feature of the dynamics. A simple exponential description of the decay, according to a Marcus type picture, is clearly not appropriate.

We still need to clarify, though, whether the origin of the observed oscillations is vibrational or electronic. To further analyze this question, the time-evolving electronic coherence

$$\rho_{\mathrm{XT,CT}}(t) = \mathrm{Tr}\{|\mathrm{CT}\rangle\langle\mathrm{XT}|\hat{\rho}(t)\} \tag{9}$$

obtained by taking the trace (Tr) over the electronic and phonon degrees of freedom of the density operator $\hat{\rho}(t) = |\psi(t)\rangle\langle\psi(t)|$, is shown in Fig. 4. The imaginary part of the coherence, $(-2\gamma/\hbar)\mathrm{Im}\rho_{\mathrm{XT,\,CT}}$, where γ is the diabatic coupling, determines the state-to-state population flux.[47] This term is seen to decay to zero after marked initial transients that are mirrored by the XT population profile. The real part of the coherence persists and indicates that the system tends towards a coherent superposition involving a non-zero admixture of the XT state ($P_{\mathrm{XT}} \sim 0.1$) to the dominant CT state ($P_{\mathrm{CT}} \sim 0.9$). Indeed, some intensity borrowing is observed for the CT state,[29,48] as supported by electronic structure calculations.[16,34]

From the above, one can conclude that electronic coherence is decisive in the initial transfer dynamics and the oscillatory features which are observed on the initial ~50 fs time scale are essentially of electronic nature. Beyond these initial transients, rapid electronic dephasing sets in due to the coupling to the vibrations. This is further borne out by the analysis of Sec. IV B, where a comparison with a purely electronic transfer dynamics is made.

Even though the coherence decay is quite rapid, the observed time scale exceeds the 10–20 fs scale that is conventionally associated with electronic decoherence. These observations are in line with various recent experimental findings on biological systems and organic materials where comparatively long-lived excitonic coherences were found.[12–14]

B. Fragment spectral densities: Thiophene vs. fullerene moieties

To analyze the role of the respective phonon distributions of the C_{60} and OT_4 fragments, we further carried out simulations of the transfer dynamics taking into account exclusively the spectral densities pertaining to one or the other fragment. Figure 5 shows these fragment spectral densities, illustrating that both moieties contribute to the low-frequency and high-frequency regions of the spectral density. As mentioned above (Sec. II), the high-frequency branch corresponds to C=S and C=C stretching and bond-length-alternation modes while the low-frequency branch comprises OT_4^+ in-plane bending modes, ring torsions, and radial fullerene H_g modes.[40] The fullerene fragment clearly dominates the high-frequency region, suggesting that the rapid electronic dephasing dynamics that were discussed above are predominantly associated with the fullerene phonon spectrum.

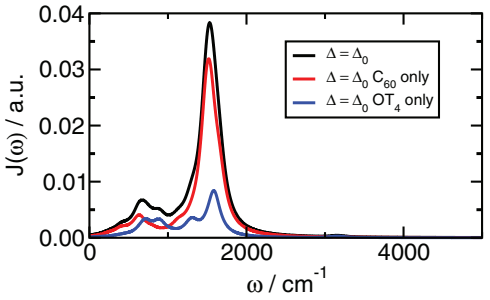

FIG. 5. Fragment spectral densities obtained by convolution of the original data shown in Fig. 2, separated for the OT_4^+ and C_{60}^- moieties. The fullerene fragment features a dominant contribution in the high-frequency region.

For reference, Fig. 6(a) shows the dynamics in the absence of any electron-phonon coupling (red trace), exhibiting purely electronic Rabi oscillations that result from the small electronic offset ($\Delta_{\mathrm{XT\text{-}CT}} = 0.079$ eV) as compared with the diabatic coupling ($\gamma = 0.13$ eV). In the presence of the inter-fragment R coordinate, as a single dynamically evolving phonon mode, the picture is modified (blue trace), leading to

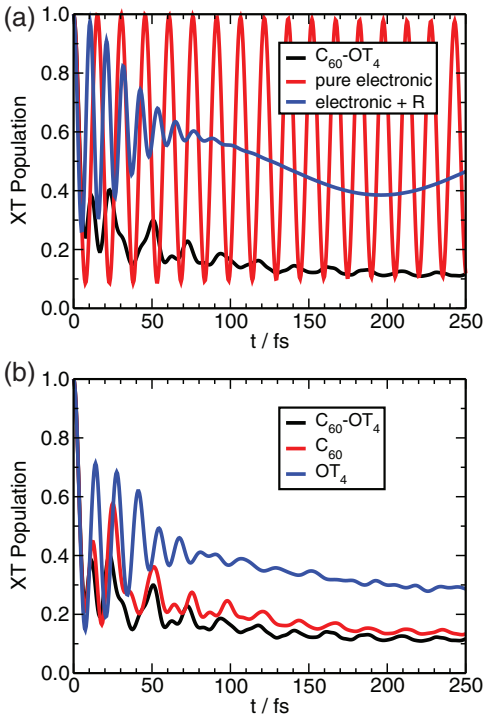

FIG. 6. (a) Transfer profiles for the pure electronic case (red trace) giving rise to Rabi oscillations, and the case where the inter-fragment mode R is included as a single phonon mode (blue trace), as compared with the full dynamics (black trace) as in Fig. 4. (b) XT state decay for the fragment spectral densities of Fig. 5. The spectral density of the C_{60} moiety generates a very similar decay as the overall phonon distribution. The simulations were carried out for $\Delta = 0.25\Delta_0$.

a decay of the Rabi oscillations. A rapid and irreversible decay is only observed, though, if a dense phonon distribution is present (black trace, cf. Fig. 4).

Figure 6(b) shows the XT decay dynamics resulting from the coupling to the inter-fragment coordinate R and the C_{60} or OT_4 phonon distributions (Fig. 5), respectively. In both cases, a rapid, oscillatory initial decay takes place, but the subsequent dynamics differ. Inclusion of the phonon distribution of the OT_4 fragment leads to a decay that qualitatively resembles the case where only R is present as an active coordinate (blue trace of Fig. 6(a)). By contrast, the spectral density of the C_{60} moiety generates a very similar decay profile as the overall phonon distribution. Even though the effects of the two fragments cannot be entirely separated, it is clear that the fullerene modes mainly determine the observed decay and lead to a population ratio on intermediate time scales (100–200 fs and beyond) that corresponds closely to the full system. Additional simulations confirm that specifically the high-frequency modes – which are mainly contributed by the C_{60} fragment – determine the transfer efficiency.

Overall, we can conclude that the earliest, very fast (∼10 fs) evolution essentially corresponds to electronic Rabi oscillations, which are subsequently modulated and damped by the coupling to the vibrations that make the evolution irreversible. Here, the fullerene modes clearly play a predominant role. This interpretation is entirely in line with the analysis of the coherent evolution in Sec. IV A.

C. Role of inter-fragment coordinate

The inter-fragment coordinate R modulates both the diabatic coupling and the energy gap between the XT and CT states, as can be inferred from the $\hat{H}_R$ portion of the Hamiltonian equation (3). Since the equilibrium geometry of the CT state is shifted to smaller R values, due to the attractive interaction of the $OT_4^+C_{60}^-$ ion pair, R will tend towards smaller values as soon as the XT → CT transition takes place. This shift towards shorter distances is in turn accompanied by an increase in the diabatic coupling (with $\gamma_R < 0$ in Eq. (3)). In the following we consider the consequence of these dependencies on the transfer dynamics.

Figure 7 compares the transfer dynamics for a static value of R, fixed at the XT state equilibrium geometry (black trace), with the full dynamics including R as a dynamically evolving

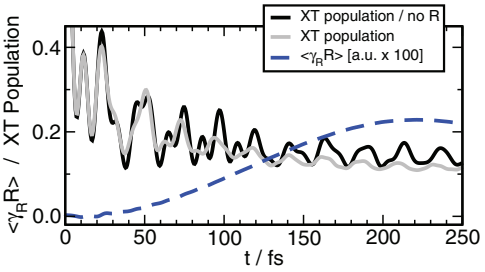

FIG. 7. XT state decay including the dynamical effects of the inter-fragment coordinate R, as compared with a simulation for R fixed at the XT state equilibrium geometry ($\langle\Delta R\rangle = 0$ a.u.). Due to the increase in the diabatic coupling as a function of the dynamics in R (see blue trace), the dynamics is increasingly anharmonic and coherent motions become less pronounced.

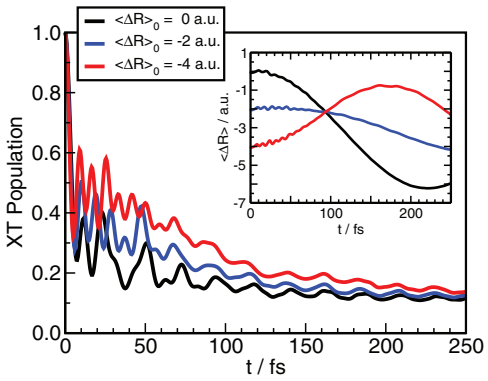

FIG. 8. Simulations for different initial conditions of the inter-fragment coordinate R, given in terms of deviations $\langle\Delta R\rangle_0$ from the XT equilibrium geometry. The case $\langle\Delta R\rangle_0 = -2$ a.u. corresponds to the CT state minimum. The inset shows $\langle\Delta R\rangle(t)$.

variable (grey trace). In the latter case, the diabatic coupling increases in the course of the evolution (blue dashed trace). As a consequence, the dynamics is increasingly anharmonic and we expect coherent motions to become less pronounced. These effects are expected to set in, though, on a time scale of hundreds rather than tens of femtoseconds, due to the comparatively low frequency of the inter-fragment mode. Therefore, the initial transfer dynamics is not strongly affected by the dynamics in the R mode. This corresponds to the observations illustrated in Fig. 7.

Another potentially important effect concerns the distribution of initial conditions as a function of R, manifesting static disorder in addition to the dynamical effects considered above. In Ref. 34, simulations were carried out for several fixed values of the inter-fragment coordinate, with significant differences in the observed dynamics beyond ∼20 fs. The pronounced sensitivity of the diabatic coupling to the R coordinate clearly affects the initial dynamics, which depends to a large extent on the electronic coupling strength. Here, we have included R as a dynamical coordinate and record the evolution as a function of different initial conditions centered on $R = R_0^{\mathrm{XT}} + \langle\Delta R\rangle_0$, see Fig. 8. The transient dynamics observed on a ∼100 fs time scale for these different initial conditions indeed differs substantially. However, the XT/CT population ratio is seen to rapidly converge around 200 fs.

Beyond these selected simulations, an appropriate sampling over a distribution of initial conditions in R will be an important ingredient for a more realistic simulation of the transfer process in the actual material.

V. CONCLUSIONS AND OUTLOOK

The combined electronic structure and dynamics analysis of Ref. 34 and the present work provide a molecular-level picture of the highly efficient and ultrafast electron transfer step at a typical oligothiophene-fullerene junction. The observed time scale of 50–100 fs is entirely in line with experimental observations.[27,28,32,33] The process is mediated by vibronic (electron-phonon) coupling – rather than thermally induced barrier crossing – as we previously showed in the analysis of a related organic heterojunction system.[23–25] The initial transient dynamics is shown to be guided by

electronic (more precisely, vibronic) coherence, which determines the observed oscillatory features of the decay dynamics. The phonon modes play an essential role in inducing dephasing and dissipating energy, thus leading to a nearly immediate and complete charge transfer. The present analysis further shows that the fullerene high-frequency modes play a predominant role in the process. At the same time, low-frequency modes are generally indispensable in providing a resonance tuning mechanism.[49–52]

By the spectral density analysis developed above, the description of electron-phonon coupling is placed into the more general context of a continuous system, which is appropriate for the actual materials to be studied. For the purpose of the present analysis, the relevant spectral density has been constructed from electronic structure information based upon an excited-state normal-mode analysis for the CT state. Other procedures could involve molecular dynamics based correlation functions whose Fourier-Laplace transforms yield the corresponding spectral densities. The combination of spectral density information with the relevant vibronic coupling matrix elements – here obtained by explicit diabatization in an *ab initio* setting – completes the molecular-level parametrization of a model Hamiltonian that is subsequently used in quantum dynamical simulations.

The MCTDH method, which has been successfully employed for the study of both vibronic coupling models and system-bath type problems,[38] provides an ideal methodology for the study of elementary quantum dynamical events in extended systems. Electronically and vibrationally coherent dynamics in many dimensions are accurately described by this method. In the present example, 60 vibrational modes were treated explicitly. Recent developments such as multi-layered MCTDH variants[53] and the effective-mode analysis of Refs. 25, 34, and 54 are useful to move towards a larger number of modes to resolve longer time scales.

While the present simulations have been carried out at zero temperature, an appropriate sampling over initial conditions would be necessary to include temperature effects. Such a sampling procedure has been carried out in Ref. 34 and led to the conclusion that temperature effects are negligible for the short-time photoinduced dynamics under study. This is confirmed by experimental observations.[32] However, sampling over a distribution of inter-fragment distances R as discussed above is necessary for a realistic description of the ensemble dynamics. In addition, the details of the interface morphology will affect the dynamical processes and need to be included on the electronic structure and dynamical modeling side.

Finally, our analysis has focused on the primary events at the donor-acceptor junction and does not include a description of photocurrent generation. Typically, tens of picoseconds are needed for the break-up of the initially formed interfacial CT state and the subsequent formation of mobile charges. On the picosecond to nanosecond time scale, geminate recombination processes interfere and significantly reduce charge migration and, hence, the net efficiency of the blend material. Approaches accounting for these processes in a framework similar to the present model have been proposed, e.g., in Refs. 22 and 55, and further work in this direction is in progress.

ACKNOWLEDGMENTS

Support by the grants-in-aid for scientific research (A) from MEXT, Japan, as well as travel support from the NAKAMA endowment fund of the University of Frankfurt are gratefully acknowledged. We thank Stephan Wefing for valuable discussions.

[1] J. J. M. Halls, J. Cornil, D. A. dos Santos, R. Silbey, D. H. Hwang, A. B. Holmes, J. L. Brédas, and R. H. Friend, Phys. Rev. B **60**, 5721 (1999).
[2] J. L. Brédas, D. Beljonne, V. Cropceanu, and J. Cornil, Chem. Rev. **104**, 4971 (2004).
[3] J. Yu, D. Hu, and P. F. Barbara, Science **289**, 1327 (2000).
[4] V. Cropceanu, J. Cornil, D. A. da Silva Filho, Y. Olivier, R. Silbey, and J.-L. Brédas, Chem. Rev. **107**, 926 (2007).
[5] S. Günes, H. Neugebauer, and N. S. Sariciftci, Chem. Rev. **107**, 1324 (2007).
[6] G. Yu, J. Gao, J. C. Hummelen, F. Wudl, and A. J. Heeger, Science **270**, 1789 (1995).
[7] P. Peumans, S. Uchida, and S. R. Forrest, Nature (London) **425**, 158 (2003).
[8] J. J. M. Halls, C. A. Walsh, N. C. Greenham, E. A. Marseglia, R. H. Friend, S. C. Moratti, and A. B. Holmes, Nature (London) **376**, 498 (1995).
[9] V. I. Arkhipov, E. V. Emelianova, and H. Bässler, Phys. Rev. Lett. **82**, 1321 (1999).
[10] A. C. Morteani, R. H. Friend, and C. Silva, in *Organic Light-Emitting Devices*, edited by K. Müllen and U. Scherf (Wiley VCH, 2006), p. 35.
[11] A. C. Morteani, A. S. Dhoot, J. S. Kim, C. Silva, N. C. Greenham, C. Murphy, E. Moons, S. Cina, J. H. Burroughes, and R. H. Friend, Adv. Mater. **15**, 1708 (2003).
[12] H. Lee, Y.-C. Cheng, and G. Fleming, Science **316**, 1462 (2007).
[13] E. Collini and G. D. Scholes, Science **323**, 369 (2009).
[14] I. Hwang and G. D. Scholes, Chem. Mater. **23**, 610 (2011).
[15] D. Beljonne, J. Cornil, L. Muccioli, C. Zannoni, J.-L. Brédas, and F. Castet, Chem. Mater. **23**, 591 (2011).
[16] Y. Kanai and J. C. Grossman, Nano Lett. **7**, 1967 (2007).
[17] B. F. Habenicht, H. Kamisaka, K. Yamashita, and O. V. Prezhdo, Nano Lett. **7**, 3260 (2007).
[18] O. V. Prezhdo, W. R. Duncan, and V. V. Prezhdo, Acc. Chem. Res. **41**, 339 (2008).
[19] T. Nelson, S. Fernandez-Alberti, V. Chernyak, A. E. Roitberg, and S. Tretiak, J. Phys. Chem. B **115**, 5402 (2011).
[20] J. Clark, T. Nelson, S. Tretiak, G. Cirmi, and G. Lanzani, Nat. Phys. **8**, 225 (2012).
[21] T. Liu and A. Troisi, J. Phys. Chem. C **115**, 2406 (2011).
[22] M. Hultell and S. Stafström, Phys. Rev. B **75**, 104304 (2007).
[23] I. Burghardt, E. R. Bittner, H. Tamura, A. Pereverzev, and J. G. S. Ramon, *Energy Transfer Dynamics in Biomaterial Systems*, Springer Series in Chemical Physics Vol. 93, edited by I. Burghardt, V. May, D. A. Micha, and E. R. Bittner (Springer, 2009), p. 183.
[24] H. Tamura, J. Ramon, E. R. Bittner, and I. Burghardt, J. Phys. Chem. B **112**, 495 (2008).
[25] H. Tamura, J. Ramon, E. R. Bittner, and I. Burghardt, Phys. Rev. Lett. **100**, 107402 (2008).
[26] N. S. Sariciftci, L. Smilowitz, A. J. Heeger, and F. Wudl, Science **258**, 1474 (1992).
[27] C. J. Brabec, G. Zerza, G. Cerullo, S. De Silvestri, S. Luzzati, J. C. Hummelen, and S. Sariciftci, Chem. Phys. Lett. **340**, 232 (2001).
[28] S. De, T. Kesti, M. Maiti, F. Zhang, O. Inganäs, A. Yartsev, T. Pascher, and V Sundström, Chem. Phys. **350**, 14 (2008).
[29] P. Parkinson, J. Lloyd-Hughes, M. B. Johnston, and L. M. Herz, Phys. Rev. B **78**, 115321 (2008).
[30] R. D. Pensack, K. M. Banyas, L. W. Barbour, M. Hegadorn, and J. B. Asbury, Phys. Chem. Chem. Phys. **11**, 2575 (2009).
[31] R. D. Pensack and J. B. Asbury, J. Phys. Chem. Lett. **1**, 2255 (2010).
[32] R. D. Pensack, K. M. Banyas, and J. B. Asbury, J. Phys. Chem. B **114**, 12242 (2010).
[33] M. Tong, N. E. Coates, D. Moses, A. J. Heeger, S. Beaupré, and M. Leclerc, Phys. Rev. B **81**, 125210 (2010).
[34] H. Tamura, I. Burghardt, and M. Tsukada, J. Phys. Chem. C **115**, 10205 (2011).

[35]J. E. Subotnik, R. J. Cave, R. P. Steele, and N. Shenvi, J. Chem. Phys. **130**, 234102 (2009).
[36]H. Köppel, W. Domcke, and L. S. Cederbaum, Adv. Chem. Phys. **57**, 59 (1984).
[37]H. Köppel, W. Domcke, and L. S. Cederbaum, in *Conical Intersections*, edited by W. Domcke, D. R. Yarkony, and H. Köppel (World Scientific, New Jersey, 2004), Vol. 15, p. 323.
[38]M. H. Beck, A. Jäckle, G. A. Worth, and H.-D. Meyer, Phys. Rep. **324**, 1 (2000).
[39]Y. Towada, T. Tsuneda, S. Yanagisawa, Y. Yanai, and K. A. Hirao, J. Chem. Phys. **120**, 8425 (2004).
[40]W. H. Green, Jr., S. M. Gorun, G. Fitzgerald, P. W. Fowler, A. Ceulemans, and B. C. Titeca, J. Phys. Chem. **100**, 14892 (1996).
[41]H. Imahori, N. V. Tkachenko, V. Vehmanen, K. Tamaki, H. Lemmetyinen, Y. Sakata, and S. Fukuzumi, J. Phys. Chem. A **105**, 1750 (2001).
[42]R. A. Marcus, Rev. Mod. Phys. **65**, 599 (1993).
[43]R. Martinazzo, K. H. Hughes, F. Martelli, and I. Burghardt, Chem. Phys. **377**, 21 (2010).
[44]H.-D. Meyer, U. Manthe, and L. S. Cederbaum, Chem. Phys. Lett. **165**, 73 (1990).
[45]U. Manthe, H.-D. Meyer, and L. S. Cederbaum, J. Chem. Phys. **97**, 3199 (1992).
[46]G. A. Worth, M. H. Beck, A. Jäckle, and H. D. Meyer, The MCTDH package, version 8.2 (2002); H.-D. Meyer, version 8.3 (2002), see http://www.pci.uni-heidelberg.de/tc/usr/mctdh/.
[47]S. Mukamel, *Principles of Nonlinear Optical Spectroscopy* (Oxford University Press, New York/Oxford, 1995).
[48]G. Grancini, D. Polli, D. Fazzi, J. Cabanillas-Gonzalez, G. Cerullo, and G. Lanzani, J. Phys. Chem. Lett. **2**, 1099 (2011).
[49]G. C. Walker, E. Akesson, A. E. Johnson, N. E. Levinger, and P. F. Barbara, J. Phys. Chem. **96**, 3728 (1992).
[50]H. Tamura, J. Chem. Phys. **130**, 214705 (2009).
[51]K. H. Hughes, C. D. Christ, and I. Burghardt, J. Chem. Phys. **131**, 124108 (2009).
[52]H. Tamura, E. R. Bittner, and I. Burghardt, J. Chem. Phys. **127**, 034706 (2007).
[53]H. Wang and M. Thoss, J. Chem. Phys. **119**, 1289 (2003).
[54]R. Martinazzo, B. Vacchini, K. H. Hughes, and I. Burghardt, J. Chem. Phys. **134**, 011101 (2011).
[55]H. Tamura and M. Tsukada, Phys. Rev. B **85**, 054301 (2012).